

DYNAMICAL CONSTRAINTS ON THE MASSES OF THE NUCLEAR STAR CLUSTER AND BLACK HOLE IN THE LATE-TYPE SPIRAL GALAXY NGC 3621

AARON J. BARTH¹, LOUIS E. STRIGARI¹, MISTY C. BENTZ¹, JENNY E. GREENE^{2,3}, AND LUIS C. HO⁴

Draft version November 24, 2018

ABSTRACT

NGC 3621 is a late-type (Sd) spiral galaxy with an active nucleus, previously detected through mid-infrared [Ne V] line emission. Archival *Hubble Space Telescope* (*HST*) images reveal that the galaxy contains a bright and compact nuclear star cluster. We present a new high-resolution optical spectrum of this nuclear cluster, obtained with the ESI Spectrograph at the Keck Observatory. The nucleus has a Seyfert 2 emission-line spectrum at optical wavelengths, supporting the hypothesis that a black hole is present. The line-of-sight stellar velocity dispersion of the cluster is $\sigma_* = 43 \pm 3 \text{ km s}^{-1}$, one of the largest dispersions measured for any nuclear cluster in a late-type spiral galaxy. Combining this measurement with structural parameters measured from archival *HST* images, we carry out dynamical modeling based on the Jeans equation for a spherical star cluster containing a central point mass. The maximum black hole mass consistent with the measured stellar velocity dispersion is $3 \times 10^6 M_\odot$. If the black hole mass is small compared with the cluster's stellar mass, then the dynamical models imply a total stellar mass of $\sim 1 \times 10^7 M_\odot$, which is consistent with rough estimates of the stellar mass based on photometric measurements from *HST* images. From structural decomposition of 2MASS images, we find no clear evidence for a bulge in NGC 3621; the galaxy contains at most a very faint and inconspicuous pseudobulge component ($M_K \gtrsim -17.6 \text{ mag}$). NGC 3621 provides one of the best demonstrations that very late-type spirals can host both active nuclei and nuclear star clusters, and that low-mass black holes can occur in disk galaxies even in the absence of a substantial bulge.

Subject headings: galaxies: active — galaxies: individual (NGC 3621) — galaxies: kinematics and dynamics — galaxies: nuclei — galaxies: spiral

1. INTRODUCTION

In the study of the demographics of supermassive black holes, one important unresolved problem is the observational census of black holes in very late-type disk galaxies. The masses of supermassive black holes in elliptical and early-type spiral galaxies appear to be well correlated with the bulge properties of their host galaxies (Kormendy & Richstone 1995; Ferrarese & Merritt 2000; Gebhardt et al. 2000). These correlations naturally lead to the question of whether supermassive black holes can form in disk galaxies that lack bulges, and if so, how the black hole mass in bulgeless galaxies might be related to the properties of the host. The nearest example of a bulgeless disk galaxy, M33, does not contain a massive black hole, with an extremely tight upper limit of $M_{\text{BH}} \lesssim 1500 - 3000 M_\odot$ determined from stellar-dynamical observations and modeling (Gebhardt et al. 2001; Merritt et al. 2001). It is not yet known whether the absence of a massive black hole is a typical property of bulgeless spirals in general, however, because very few late-type disk galaxies are near enough for stellar-dynamical measurements to yield such stringent constraints on the black hole mass.

It has long been recognized that many spiral galaxies contain photometrically and dynamically distinct central star-cluster nuclei, with the M33 nucleus being one of the best-studied examples (e.g., Walker 1964; van den Bergh 1976; Gallagher et al. 1982; Nieto & Aurière 1982; O'Connell 1983). The *Hubble Space Telescope* (*HST*) made it possible

to survey the properties of nuclear star clusters in more distant galaxies (e.g., Phillips et al. 1996; Carollo et al. 1997), and *HST* imaging programs have demonstrated that the majority of very late-type spirals (Hubble types Scd–Sd) contain compact star-cluster nuclei at or very close to their isophotal centers (Matthews et al. 1999; Böker et al. 2002). Spectroscopic observations have revealed that the nuclear clusters in late-type spirals typically have stellar velocity dispersions of $\sim 15 - 35 \text{ km s}^{-1}$ (Böker et al. 1999; Walcher et al. 2005), effective radii of a few parsecs (Böker et al. 2004), and dynamical masses of $\sim 10^6 - 10^7 M_\odot$ (Böker et al. 1999; Walcher et al. 2005). The spectra also reveal composite stellar populations indicative of multiple star formation episodes, with most clusters containing a population component with an age of $\lesssim 100 \text{ Myr}$ (Walcher et al. 2006; Rossa et al. 2006).

The discovery of scaling relationships between nuclear cluster masses and host galaxy properties, both in spirals (Rossa et al. 2006) and in dwarf ellipticals (Wehner & Harris 2006; Ferrarese et al. 2006), offers an intriguing hint of a connection between the processes that govern the growth of nuclear clusters and black holes. Ferrarese et al. (2006) speculate that the formation of nuclear star clusters and massive black holes might be mutually exclusive, such that black holes are able to form only in galaxies above some critical mass. However, the only nuclear star clusters in which the presence of a massive black hole can be ruled out at any significant level are in the Local Group or within a few Mpc. Optical spectroscopic surveys have shown that active galactic nuclei (AGNs) do occur in some nuclear star clusters in nearby galaxies (Seth et al. 2008a), so black holes and nuclear clusters can apparently coexist. Evidence that black holes can occur in at least some very late-type disk galaxies comes from the detection of a small number of AGNs in Scd and Sd-type spirals. The best example is the Sd galaxy NGC 4395,

¹ Department of Physics and Astronomy, 4129 Frederick Reines Hall, University of California, Irvine, CA 92697-4575; barth@uci.edu

² Department of Astrophysical Sciences, Princeton University, Princeton, NJ 08544

³ Hubble Fellow and Princeton-Carnegie Fellow

⁴ The Observatories of the Carnegie Institution of Washington, 813 Santa Barbara Street, Pasadena, CA 91101

which contains a Seyfert 1 nucleus (Filippenko & Sargent 1989; Filippenko & Ho 2003); it remains the only clear identification of a broad-lined AGN in a bulgeless disk galaxy. In addition, a few examples of Type 2 AGNs in very late-type spirals have been detected recently in optical spectroscopic surveys, such as NGC 1042 (Seth et al. 2008a; Shields et al. 2008) and UGC 6192 (Barth et al. 2008). In both NGC 4395 and NGC 1042 the AGNs occur in nuclear star clusters (it is not known whether UGC 6192 contains a nuclear cluster).

A recent *Spitzer* spectroscopic observation of the Sd galaxy NGC 3621 by Satyapal et al. (2007) led to the discovery of an active nucleus, based on the detection of [Ne V] emission lines at $14.3 \mu\text{m}$ and $24.3 \mu\text{m}$. Since photon energies greater than 95 eV are required for photoionization of Ne^{+3} to Ne^{+4} , ordinary H II regions are not expected to be significant sources of [Ne V] emission, but a hard AGN continuum can easily provide the necessary ionizing photons. Emission lines from a range of ionization states of neon are observable in the mid-infrared, and the relative strengths of these lines are useful as diagnostics of the ionization conditions within AGN narrow-line regions (e.g., Spinoglio & Malkan 1992; Voit 1992; Sturm et al. 2002; Groves et al. 2006). Abel & Satyapal (2008) used the results of new photoionization models to argue that the strength of the [Ne V] emission in NGC 3621 can only be plausibly explained by the presence of an AGN, and not by an ordinary burst of nuclear star formation. The detection of an AGN in NGC 3621 is of significant interest because it is one of the few very late-type spirals known to host an active nucleus, making it an important target for further observations to constrain its black hole mass and AGN energetics. Satyapal et al. (2007) note that there is no previously published optical spectrum of the nucleus of NGC 3621 suitable for emission-line classification.

In this paper, we use archival *HST* images to show that NGC 3621 contains a well-defined and compact nuclear star cluster. A new optical spectrum of this star cluster is used to examine the classification of the active nucleus, and to measure the stellar velocity dispersion of the cluster. We describe dynamical modeling of the nuclear cluster and the resulting constraints on the masses of both the cluster and the central black hole. We also examine the structure of NGC 3621 using near-infrared images from 2MASS in order to search for a bulge component in this late-type galaxy. For the distance to NGC 3621, we adopt $D = 6.6$ Mpc, based on the Cepheid measurements of Freedman et al. (2001). At this distance, $1''$ corresponds to 32.0 pc.

2. IMAGING DATA

2.1. Archival *HST* Data

NGC 3621 has been observed numerous times with *HST*, although many of the observations were of outer fields that do not include the nucleus, taken as part of the *HST* Key Project on the Cepheid distance scale (Freedman et al. 2001). We found three sets of images that did cover the galaxy nucleus: one with WFPC2, one with ACS, and one with NICMOS. The parameters for each of these observations are listed in Table 1. The galaxy was observed with ACS/WFC at two separate pointings. One ACS pointing placed the nucleus on the WFC1 CCD and the other pointing placed it on the WFC2; at both positions, identical exposure sequences were obtained in three filters. We selected the WFC1 pointing since this image included a larger region surrounding the nucleus. The NICMOS F190N exposure was taken as the continuum observation for

TABLE 1
HUBBLE SPACE TELESCOPE ARCHIVAL DATA

Camera	Filter	Exposure Time (s)	Observation Date
WFPC2/PC	F606W	2×80	1994-08-17
ACS/WFC1	F435W	3×360	2003-02-03
	F555W	3×360	2003-02-03
	F814W	3×360	2003-02-03
NICMOS/NIC3	F190N	6×224	2007-03-31

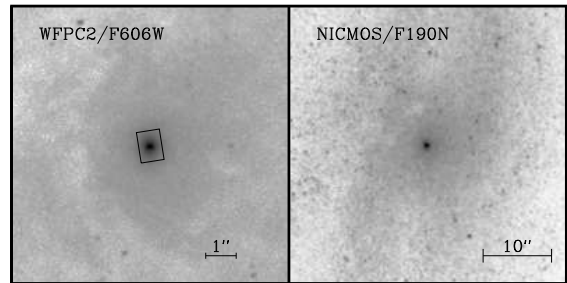


FIG. 1.— *HST* images of the nucleus of NGC 3621. *Left panel*: A portion of the WFPC2/PC F606W image. The rectangle surrounding the nucleus shows the position and size of the spectroscopic aperture used in the Keck observation, for the $1''$ -wide extraction described in §3.1. *Right panel*: A portion of the NICMOS/NIC3 F190N image, with a larger field of view displayed. In both panels, north is up and east is to the left.

an F187N (Paschen α) narrow-band image. We do not use the F187N emission-line image here.

The NICMOS and ACS images were retrieved from the *HST* data archives and we use the standard pipeline-processed versions of these images. For the WFPC2 data, we use the cosmic-ray cleaned and co-added image from the WFPC2 Associations archive.

Figure 1 displays the central regions of the WFPC2 and NICMOS images. The images show that the galaxy contains a very compact and photometrically distinct nuclear star cluster. Surrounding the cluster is a smooth and nearly featureless region of radius $\sim 1''.5$ (or ~ 50 pc). At larger radii, dust lanes and young star clusters become more prominent in the optical images, especially in the ACS F435W band.

2.1.1. GALFIT Modeling

To determine the structure of the nuclear cluster, we use the 2-dimensional modeling package GALFIT (Peng et al. 2002). Unfortunately, the nuclear star cluster is saturated in the ACS/WFC F555W and F814W images, making it impossible to use these images to derive structural parameters for the cluster. The ACS F435W image is not saturated, but in this blue passband the dust lanes and massive stars in the circumnuclear region are more prominent, making this band less easily suited to modeling. In the NICMOS image (with a scale of $0''.2 \text{ pixel}^{-1}$), the cluster is unresolved. Therefore, we use the WFPC2/PC image for the GALFIT decomposition. WFPC2 magnitudes listed below are on the Vegamag system, using a zeropoint of 22.887 for the F606W filter (Baggett et al. 1997).

For the GALFIT modeling, we extracted a $101 \times 101 \text{ pixel}^2$ region from the PC image, centered on the nuclear cluster. This corresponds roughly to the smooth region surrounding the cluster. A larger region would be less suitable for GALFIT modeling because of the increasing prominence of the dust lanes at larger distances from the nucleus. A few patches or lanes of dust are visible at the edges of this extracted image, and we created a mask image to exclude these regions from the GALFIT optimization. For the point-spread func-

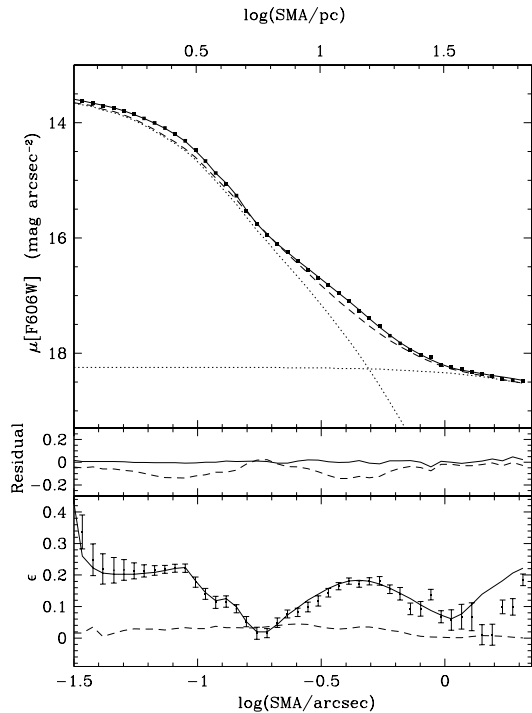


FIG. 2.— Radial profiles of surface brightness and ellipticity for the nuclear cluster in the WFPC2/PC F606W image. “SMA” denotes the semi-major axis of the fitted elliptical isophotes. The individual data points represent the radial profile measured from the *HST* image. The long-dashed curve is the radial profile of the circularly symmetric GALFIT model, and the solid curve is the radial profile of the model fit that was not constrained to have circular symmetry. Dotted curves show the radial profiles for the disk and cluster separately, for the symmetric model. The middle panel shows the model residuals for the radial profile fit (in mag arcsec^{-2}). The slight departures from zero ellipticity in the circularly symmetric model are due to random errors in the ellipse fitting to the GALFIT model.

tion (PSF) model, we used the Tiny Tim package (Krist 1993) to create a PSF for the WFPC2/PC camera and F606W filter, at $2\times$ oversampling. In GALFIT, the galaxy model is created on an oversampled grid, convolved with the PSF model, and finally resampled back to the WFPC2/PC plate scale and convolved with the WFPC2 CCD charge-diffusion kernel (Krist 1993) in order to compare with the observed galaxy image.

As an initial step, we attempted to model the image as the sum of an exponential disk plus a central cluster, using a variety of possible models for the cluster based on the various functional forms available in GALFIT (Gaussian, Moffat function, Sérsic function, and King model). None could adequately represent the cluster profile; in each case there were large systematic residuals. After much experimentation we took a different approach, modeling the cluster as a sum of several Gaussian components, since a superposition of a sufficient number of Gaussians can in principle be used to fit an arbitrary cluster profile. As a simplifying step, we constrained the Gaussian components and exponential disk to be concentric in the GALFIT model, and found that we were still able to fit the cluster profile adequately with this restriction. We began with an exponential disk plus a single Gaussian component and added additional Gaussians until the model profile ceased to improve significantly with the addition of a further component. In our final model we use five Gaussian components plus an exponential disk.

We created two versions of this GALFIT model. In the first, the individual Gaussian components were forced to be con-

centric and circularly symmetric (i.e., axis ratio $b/a = 1$). This model lends itself most easily to deprojection and dynamical modeling, but might not yield an acceptable fit to the cluster structure. In the second version, the individual components were still set to be concentric, but we allowed each Gaussian component to have arbitrary values of axis ratio and position angle.

We used the IRAF⁵ `ellipse` task to examine the radial profile of the cluster and GALFIT models; this task uses the elliptical isophote fitting method described by Jedrzejewski (1987). Figure 2 illustrates the results. We find that the two models (symmetric and asymmetric) have nearly identical radial profiles. The asymmetric model yields an excellent match to the cluster’s ellipticity profile (with ellipticity ranging from ~ 0.015 to 0.38 within the inner $r < 2''$). Although the symmetric model is obviously unable to match the ellipticity profile of the cluster, the azimuthally-averaged surface brightness profile of the symmetric model is very similar to that of the cluster itself, as seen in Figure 2. This makes it possible to use a deprojected version of the symmetric model as a simplified, spherically-symmetric representation of the cluster structure (see §4).

In the spherical model, the individual Gaussian components have FWHMs of 1.8, 4.3, 9.9, 20.9, and 69.7 pixels (with an image scale of $0''.045 \text{ pixel}^{-1}$). The three narrowest components contribute the majority of the cluster’s light. The broadest Gaussian component from the GALFIT decomposition has an extent (FWHM=69.7 pixels or $3''.1$) much larger than the visible size of the cluster in the WFPC2 image, and we conclude that it represents light belonging predominantly to the galaxy disk rather than to the cluster. As we show below in §4, the choice of whether to assign this component to the cluster or the disk has a very small effect on the dynamical modeling results. The next-broadest component, with FWHM= $0''.94$, has a size comparable to the wings of the cluster visible in the WFPC2 image (as well as being similar in size to our spectroscopic aperture). We interpret this component as belonging to the cluster, although the distinction between cluster and disk becomes ambiguous in the outer wings of this component and there is no clear way to determine the outermost extent of the cluster.

The F606W magnitudes of these five Gaussian components are 17.86, 18.29, 17.97, 18.09, and 17.18 mag, respectively. If we represent the cluster by the sum of the first four Gaussian components, then its half-light radius is $0''.13$, corresponding to 4.2 pc. Böker et al. (2004) find that 50% of nuclear clusters in late-type spirals have r_e between 2.4 and 5.0 pc, so the size of the NGC 3621 nuclear cluster is very typical for this class of objects. The exponential component in the GALFIT decomposition has a scale length of $23''$ and a magnitude of $m_{\text{F606W}} = 9.7$ mag, corresponding to $V \approx 10.0$ mag based on an estimated color of $(\text{F606W} - V) = -0.3$ mag for an Sc galaxy template (Kinney et al. 1996). Since the GALFIT fitting was carried out over only the central $4''.5 \times 4''.5$ of the galaxy, there is no reason to expect this component to be an accurate representation of the primary exponential disk of the entire galaxy, but its magnitude is surprisingly close to the galaxy’s total V magnitude of 9.5 mag as listed in the HyperLeda catalog (Paturel et al. 2003).

⁵ IRAF is distributed by the National Optical Astronomy Observatories, which are operated by the Association of Universities for Research in Astronomy, Inc., under cooperative agreement with the National Science Foundation.

The radial profile plot shown in Figure 2 shows that the observed (i.e., PSF-convolved) surface brightness falls by ~ 5 mag arcsec $^{-2}$ within the inner $r = 1$ arcsec of the galaxy profile, where the cluster outskirts have essentially merged into the surrounding disk. Such a large gradient in surface brightness over such a small radius places this object among the most solidly detected nuclear clusters, in comparison with the late-type spirals from the Böker et al. (2002) sample.

2.1.2. Aperture Photometry

Unfortunately, the saturation in the ACS F555W and F814W images precludes their use for GALFIT modeling or aperture photometry of the nuclear cluster. If the default ACS/WFC GAIN=2 setting had been used for these observations, it would still have been possible to perform accurate aperture photometry on mildly saturated objects. With GAIN=2, saturation of the CCD full well results in charge-bleeding onto adjacent pixels while still conserving the total count rate for the object (Gilliland 2004). However, the NGC 3621 images were taken with GAIN=1, which does not sample the CCD full well capacity, and in this situation the photometry of saturated objects is compromised. This leaves the ACS F435W, WFC2 F606W, and NICMOS F190N observations as the only usable *HST* images. The NICMOS image has a much coarser plate scale ($0''.2$ pixel $^{-1}$) and a much broader PSF than the optical images, and the impact of dust lanes is very different between the optical and near-infrared images, and as a result it would be very difficult to carry out GALFIT modeling in a consistent manner for all of these images. Therefore, we fall back on a simpler strategy, in which we perform aperture photometry to measure the cluster’s brightness in each image.

Under the assumption that the narrowest four Gaussian components from the GALFIT model represent the light of the cluster, 90% of the cluster’s light (in projection) is contained within a circular aperture of radius 12 pixels, or $0''.54$. We use this as the fiducial aperture radius for the photometric measurements, since at larger radii it becomes very difficult to distinguish between the outskirts of the cluster and the surrounding galaxy disk. For the photometry, we set the background annulus close to the cluster, in order to minimize uncertainties due to the gradient in the fairly flat light profile of the host galaxy, and we use a background region of $0''.6 < r < 1''.0$. For the two optical images, we find *HST* filter magnitudes for the cluster of $m_{F435W} = 17.82$ and $m_{F606W} = 16.75$ mag (both given on the Vega system). Uncertainties on these measurements are dominated by the choice of the inner and outer background radii (rather than photon-counting statistics), and we estimate overall uncertainties of ~ 0.1 mag on each measurement based on varying the inner and outer radii of the background region over wider radial ranges. Using the IRAF SYNPHOT package, we can convert these *HST* filter magnitudes to Johnson *B* and *V* magnitudes. For a wide range of spectral shapes corresponding to S0–Sc galaxy templates (Kinney et al. 1996), the (F606W–*V*) color index is -0.32 ± 0.02 mag. The ACS F435W filter is very close to a Johnson *B* passband, and SYNPHOT calculates a color index of (F435W–*B*) = 0.03 ± 0.01 mag for the Kinney et al. (1996) templates. Correcting for Galactic extinction based on $E(B-V) = 0.08$ mag (Schlegel et al. 1998), we have $M_B = -11.65$ and $M_V = -12.30$ mag for the cluster, not including any correction for internal extinction within the host galaxy or the cluster itself.

We carried out photometry using the same aperture and

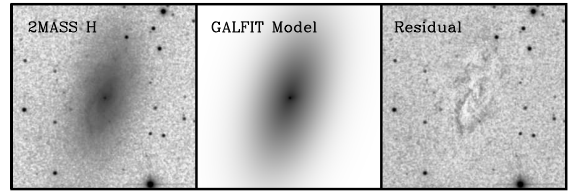


FIG. 3.— *Left panel:* 2MASS *H*-band image of NGC 3621. *Center panel:* GALFIT model. *Right panel:* GALFIT residuals. The image size is $5' \times 5'$. North is up and east is to the left.

background radii on the NICMOS image, but an additional aperture correction was required in order to use photometry through an aperture of the same physical size, because the NICMOS NIC3 PSF contains significant flux at radii larger than $0''.54$. To estimate the aperture correction, we created a GALFIT model of the nuclear cluster at the plate scale of the NIC3 camera, using the components from the WFC2 GALFIT model, and convolved the model with a NIC3 PSF generated by Tiny Tim. We then carried out aperture photometry on the simulated cluster image in an $0''.54$ aperture, and determined the aperture correction needed to correct that photometric measurement to one that would correspond to 90% of the total cluster light (to be consistent with the optical measurements). The resulting aperture correction was 0.23 mag. Applying the NICMOS photometric zeropoint to the aperture-corrected photometric measurement, we find a flux density in the F190N filter of $f_\nu = 2.4 \times 10^{-26}$ ergs cm $^{-2}$ s $^{-1}$ Hz $^{-1}$ at 19000 Å, corresponding to an AB magnitude of 15.43 or a Vega magnitude of 13.83 mag.

2.2. 2MASS Data

To determine the overall structure of the galaxy, we examine images from the 2MASS survey (Skrutskie et al. 2006). Of the three 2MASS bands, the *H*-band image of NGC 3621 has the best *S/N* and image quality, and we used this image to create the primary GALFIT model. The image scale is $1''$ pixel $^{-1}$, corresponding to 32 pc pixel $^{-1}$. While the nuclear cluster is unresolved in the 2MASS images, it is still visible as a distinct, compact peak in the galaxy center.

We created a PSF model for the 2MASS image using the PSF task in the IRAF DAOPHOT package, combining the profiles of 42 individual isolated stars from the image. The resulting PSF model is well fit by a Moffat function with $\text{FWHM} = 2''.89$.

To construct a GALFIT model of the galaxy, we started with a single exponential disk component and added additional components as needed to eliminate strong systematic residuals. A three-component model (convolved with the PSF) proved to be the minimal model that yielded an acceptable fit, with the three components describing the primary disk, an inner disk or possible bulge component, and the nuclear cluster. We used a Sérsic model for the possible bulge component. With the Sérsic index n left to vary freely in the fit, both n and r_e for this component converged to extremely large and unreasonable values. To better constrain the model, we carried out the fit with the Sérsic index n of the inner component fixed to values 1, 2, 3, and 4, and the model with $n = 1$ (i.e., an exponential profile) yielded the lowest χ^2 . We modeled the nuclear cluster as an unresolved source and found an acceptable fit with no strong residuals at the location of the nucleus. The 2MASS image, best-fitting model, and fit residuals are shown in Figure 3, and the galaxy radial profile is shown in Figure 4. Magnitudes for each model component are listed in Table 2. For the outer exponential disk, we find a scale length

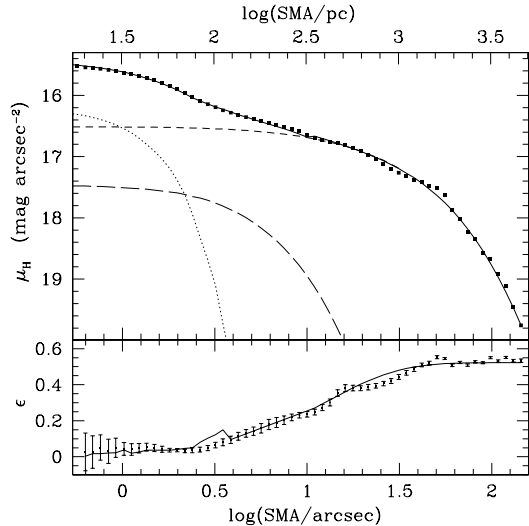


FIG. 4.— Radial surface brightness profile (upper panel) and ellipticity profile (lower panel) measured from the 2MASS H -band image using the IRAF `ellipse` task. The individual points show the profile of the 2MASS image, and the solid curve is the full galaxy model. Individual model profiles are shown for the nuclear cluster (dotted line), inner exponential (long-dashed line), and outer exponential component (short-dashed line). The nuclear cluster is modeled as an unresolved source and this component illustrates the radial profile of the PSF image.

TABLE 2
2MASS GALFIT FITTING RESULTS

Component	J	H	K
Primary Disk	7.61	6.96	6.71
Inner Sérsic ($n = 1$)	12.65	11.73	11.47
Nucleus	14.14	13.53	13.32

NOTE. — All results are given in magnitudes, on the 2MASS photometric system.

of $h = 45''.6$ (or 1.46 kpc) and axis ratio of $b/a = 0.48$. For the inner Sérsic component with $n = 1$, the model yields $r_e = 9''.6$ (or 307 pc), and $b/a = 0.64$.

Following the same procedures, we created PSF models for the 2MASS J and K -band images, and ran GALFIT on the J and K images using the best-fitting H -band model parameters as an initial input to the fit. The fits were very similar to the H -band results, and the component magnitudes are listed in Table 2. As is typically the case for GALFIT decompositions, the formal fitting errors returned by GALFIT are extremely small (< 0.02 mag) and only reflect the statistical uncertainties on the best-fit model. The actual uncertainties on each component magnitude are dominated by systematic errors, typically driven by real structural differences between the galaxy’s light profile and the idealized GALFIT model (such as overall asymmetries, dust lanes, and spiral structure), and are probably at least 0.1 mag.

The primary exponential disk is the dominant component of the galaxy, containing 99% of the total H -band light in the galaxy model. Our fitting results demonstrate that the galaxy does not contain any substantial bulge component, and possibly no bulge at all. At best there is a minor plateau in the inner disk surface brightness, corresponding to the inner Sérsic component in the GALFIT fits, that might possibly be ascribed to a faint pseudobulge. The central surface brightness of this inner exponential component is 1 mag arcsec $^{-2}$ fainter

than the surface brightness of the primary (outer) disk component.

The inner Sérsic component does have some properties in common with pseudobulges. It is best fit with an exponential profile ($n = 1$), which is typical for pseudobulges in spiral galaxies (Andredakis & Sanders 1994; Andredakis et al. 1995). Furthermore, the ratio of its effective radius to the scale length of the primary disk is $r_e/h = 0.21$, consistent with the mean $\langle r_e/h \rangle = 0.22 \pm 0.09$ found by MacArthur et al. (2003) for a large sample of late-type spirals containing pseudobulges. With an absolute magnitude of $M_H = -17.4$, $M_K = -17.6$ mag, the luminosity of the inner exponential component is within the range spanned by pseudobulges in nearby disk galaxies (Carollo et al. 2001) as well. The inner Sérsic component also has a smaller ellipticity than the primary disk, suggestive of a bulge-like feature; this is also seen as the gradual increase in ellipticity with radius in the H -band radial profile (Figure 4). Nevertheless, this component is so faint relative to the primary disk that it is uncertain whether it represents a distinct physical component of the galaxy. Since its interpretation is somewhat uncertain, we take its luminosity to be an upper limit to the luminosity of a bulge or pseudobulge in NGC 3621. Deeper and higher-resolution infrared observations would still be desirable, in order to carry out a more definitive search for a faint bulge component in this galaxy.

One possible concern in these model fits is that a small bulge, nearly unresolved in the 2MASS images, might be subsumed within the nuclear cluster component in the model fits. However, the small size of this component makes this unlikely, because the majority of the light in the unresolved nuclear component is contained within the inner $r = 2$ pixels (64 pc). Still, to test for the presence of non-cluster light in the nuclear GALFIT component, we compared the 2MASS fitting results to the small-aperture HST NICMOS F190N measurement of the nuclear cluster brightness. The NICMOS aperture photometry results in $f_\nu = 2.4 \times 10^{-26}$ ergs cm $^{-2}$ s $^{-1}$ Hz $^{-1}$ at 19000 Å. Converting the nuclear cluster magnitudes from the 2MASS GALFIT models ($H = 13.52$, $K = 13.32$) to flux densities, we find $f_\nu(1.65 \mu\text{m}) = 4.0 \times 10^{-26}$ and $f_\nu(2.2 \mu\text{m}) = 3.0 \times 10^{-26}$ ergs cm $^{-2}$ s $^{-1}$ Hz $^{-1}$, in each case somewhat larger than the NICMOS flux. This suggests that there may be some contribution of non-cluster light included in the nuclear cluster component in the GALFIT models, which would not be surprising given the coarse pixel scale of the 2MASS images. Still, the amount of possible “extra” non-cluster light in the nuclear cluster model component is well below the brightness of the inner exponential component in the GALFIT models, and the upper limits to the bulge luminosity described above are not affected.

2.3. Stellar Mass Estimates

The stellar mass of the cluster is a quantity of primary interest. Ideally, the stellar mass would be determined from HST photometry using the widest possible wavelength coverage, from the ultraviolet to near-infrared, as well as stellar population fits to spectroscopic data, in order to minimize degeneracies between age, metallicity, and reddening. In addition, the stellar population is expected to be composite, containing a wide range of stellar ages, as seen in other nuclear clusters. The accuracy of our estimates is very limited with only three photometric bands available. The lack of photometric coverage blueward of the B band exacerbates the problem, since U -band or near-UV measurements would be needed to accurately constrain the presence of a young stellar population

component in the cluster. Furthermore, the available spectroscopic data (described below) has very low S/N blueward of $H\beta$, making it unsuitable for the sort of detailed stellar population modeling that was done by Walcher et al. (2006) and Rossa et al. (2006) for other nuclear clusters.

To estimate the cluster’s stellar mass, we used the `kcorrect` package (version 1.4; Blanton & Roweis 2007), which performs fits of model spectral energy distributions for composite stellar populations with varying amounts of reddening to photometric data in arbitrary filter sets. The code uses a basis set of instantaneous-burst spectra from the models of Bruzual & Charlot (2003) with the Chabrier (2003) initial mass function, and finds the best-fitting match of the spectral templates to the photometric data using a nonnegative matrix factorization technique. To input our photometric data points into `kcorrect`, we correct them for Galactic extinction ($A = 0.33, 0.22,$ and 0.04 mag in the F435W, F606W, and F190N filters, respectively), and convert to AB magnitudes. The code returns a best-fitting mass-to-light ratio of 0.47 (in solar units) in the NICMOS F190N band, and a stellar mass of $M_* = 1.5 \times 10^7 M_\odot$ based on the cluster light within the $0''.54$ photometric aperture. Combining the mass estimate from `kcorrect` with the cluster’s V -band luminosity, we have a V -band mass-to-light ratio of $(M/L)_V = 2(M_\odot/L_{\odot,V})$.

To obtain an additional estimate of the stellar mass from the photometric measurements, we applied the results of Bell et al. (2003) to derive a K -band mass-to-light ratio based on the optical color measured from the ACS and WFPC2 images. The Bell et al. (2003) M/L values are based on the PEGASE spectrophotometric evolution models (Fioc & Rocca-Volmerange 1997), assuming an exponentially declining star-formation rate. The assumed stellar initial mass function (IMF) is a modified Salpeter (1955) IMF with a smaller contribution from low-mass stars, resulting in a 30% reduction in mass relative to a Salpeter IMF for a given luminosity. Bell et al. estimate that their M/L ratios may have $\sim 20\%$ random uncertainties and $\sim 25\%$ systematic uncertainties due to dust extinction and differences in galaxy ages and star-formation histories. Uncertainties in the IMF are likely to contribute at least this much systematic error as well.

Transforming the optical photometry to Johnson filters, we find $(B-V) \approx 0.6$ mag for the cluster. For this color index, the Bell et al. results predict $(M/L)_K = 0.75$ in solar units. Applying this mass-to-light ratio to the point source component in the 2MASS K -band model gives a stellar mass of $3 \times 10^7 M_\odot$. As discussed above, the comparison between NICMOS and 2MASS photometry of the nuclear cluster suggests that the 2MASS K magnitude might be too bright by $\sim 20\%$ due to inclusion of non-cluster light. The Bell et al. prescriptions yield a V -band stellar mass-to-light ratio of $(M/L)_V = 1.4(M_\odot/L_{\odot,V})$, and combining this with the absolute V magnitude determined from the WFPC2 data implies $M_* = 1.0 \times 10^7 M_\odot$. From all of these results, our best estimate of the cluster’s stellar mass is $\sim (1-3) \times 10^7 M_\odot$.

These stellar masses are highly uncertain due to the limited spectral coverage of the *HST* data. Even with a more complete dataset, however, there are potentially large systematic uncertainties in stellar masses obtained by these techniques. As discussed by Kannappan & Gawiser (2007), different methods for estimating galaxy stellar masses (i.e., from spectral energy distribution model fitting with different evolutionary synthesis models, or from the Bell et al. M/L calibration) can result in systematic differences of at least a factor of 2, and possibly more than a factor of 3, even when the same IMF

is assumed. Allowing for uncertainty in the IMF, a systematic uncertainty of more than a factor of 4 in stellar mass is certainly plausible, particularly in view of the complex star formation history of a typical nuclear star cluster. Ultimately, the main conclusion that we can draw from these results is that within the substantial uncertainties, the stellar mass derived from the *HST* photometry appears to be consistent with the cluster’s dynamical mass (as described below in §4).

3. SPECTROSCOPIC DATA

3.1. Observations and Reductions

A 600 s exposure of the nucleus of NGC 3621 was obtained at the Keck-II telescope on the night of 2008 March 2 with the Echelle Spectrograph and Imager (ESI; Sheinis et al. 2002). An $0''.75$ -wide slit was used in ESI echelle mode, and the slit was oriented at the parallactic angle ($PA=9^\circ$). The instrumental dispersion with this slit width is $\sigma_i \approx 22$ km s $^{-1}$, and the pixel scale in the dispersion direction is 11.5 km s $^{-1}$ pixel $^{-1}$, with total wavelength coverage of 3850–11000 Å over 10 echelle orders. We do not have a direct measurement of the seeing during the exposure (taken at air-mass 1.62), but the seeing in standard star observations on that night was $\sim 0''.8-1''.2$. Extracted spectra were wavelength-calibrated using observations of HgNe, Xe, and CuAr comparison lamps, and flux-calibrated with an observation of the standard star Feige 34. Error spectra were extracted and propagated through the same sequence of calibrations.

We performed the spectral extractions twice using different extraction widths. To obtain a spectrum of the nuclear cluster, we extracted the spectrum using an extraction width of $1''$, and a background region of $2''.5-5''.0$ on either side of the nucleus. This small-aperture spectrum did not yield satisfactory results for the emission lines, however. The emission lines are extended over a region of several arcseconds along the slit, and the emission-line surface brightness is not centrally concentrated. Consequently, the small-aperture extraction included only a small fraction of the total emission-line flux in the slit, and the close-in background regions had nearly the same emission-line surface brightness as the extraction window. In the resulting spectrum, the emission lines had erroneously low fluxes due to this background subtraction problem. To obtain a better emission-line spectrum, we performed another extraction using a $5''$ extraction width, with the background regions close to the edges of the slit where the emission-line surface brightness is lower. We use the narrow extraction in §3.2 below for measurement of the nuclear cluster’s velocity dispersion, and the wider extraction in §3.3 to examine the nuclear emission-line ratios.

3.2. Stellar Kinematics

The velocity dispersion of the nuclear star cluster was measured with the direct-fitting routine described by Barth et al. (2002), using spectra of four stars of spectral type G8III–K2III observed during the same run. We performed fits separately to spectral regions around Mgb (5100–5450 Å) and the Ca II triplet lines (CaT; 8400–8750 Å). The fitting routine models the galaxy spectrum as the sum of a stellar spectrum broadened by a Gaussian kernel and a power-law featureless continuum. The velocity-broadened spectrum is multiplied by a quadratic polynomial that can account for both reddening and minor differences in flux calibration between the galaxy and template star. The resulting spectrum is then fitted to the data, with the velocity dispersion, power-law slope and nor-

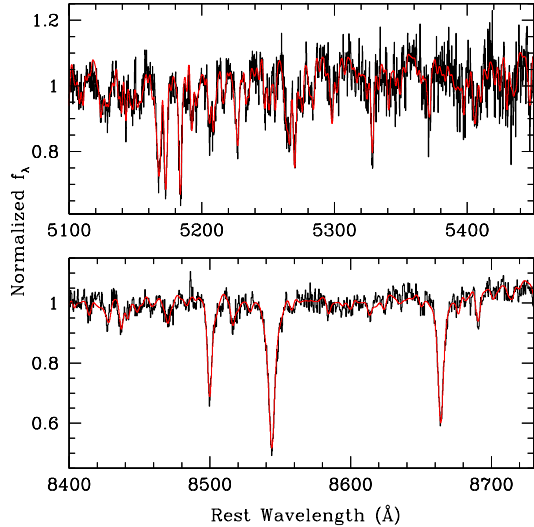


FIG. 5.— Spectral regions used for measuring the stellar velocity dispersion. The red curve is the best-fitting velocity-broadened template star spectrum.

malization, and multiplicative polynomial parameters allowed to vary as free parameters in the fit. The measurements for the blue and red spectral regions yielded identical results of $\sigma = 43 \pm 3 \text{ km s}^{-1}$, where the uncertainty represents the sum in quadrature of the fitting error on the best-fitting template and the standard deviation of the velocity dispersions derived from all template stars. Figure 5 shows the template fits to the spectrum of the nuclear cluster. The Gaussian-broadened template spectrum fits the profiles of the strong Ca II lines well, indicating that the possible contribution of higher-order moments to the line-of-sight velocity profile is relatively insignificant for the integrated spectrum of the cluster.

For the blue spectral region, differences in the the Fe/ α abundance ratio between the galaxy and the template stars can potentially lead to biased results, because the strongest features immediately redward of Mgb are Fe features such as Fe5270. The direct-fitting routine requires the featureless continuum dilution to vary smoothly with wavelength, and it cannot properly account for strong differences in line strength between adjacent Fe and Mg features (see Barth et al. 2002 for further details). However, in this case we found that the fitting results were not sensitive to whether the Mgb lines were included or masked out in the fit, and Figure 5 shows that the routine yields a good fit over the entire 5100–5450 Å region. As an additional check, we also measured the velocity dispersion using an independent direct-fitting code described by Greene & Ho (2006a) and found very consistent results (44 ± 2 and $43 \pm 2 \text{ km s}^{-1}$ for the Mgb and CaT regions, respectively). We adopt $\sigma_* = 43 \pm 3 \text{ km s}^{-1}$ as the best estimate of the line-of-sight stellar velocity dispersion.

The ESI slit length of $20''$ is too short to obtain a pure sky spectrum simultaneously with the galaxy observation, and it is unavoidable that the background regions used for sky subtraction contain light from the galaxy disk. Consequently, the background subtraction employed in the spectral extraction must be subtracting off some galaxy light with a different velocity dispersion and possibly a different mean velocity than that of the cluster itself. We tested the magnitude of this effect using the data from the ESI echelle order containing Mgb and Fe5270. For this order, we added the extracted sky spectrum back into the extracted cluster spectrum, to obtain a spectrum

of the cluster without sky subtraction. We then ran the velocity dispersion fitting routine on this spectrum. The result was an increase of only 1 km s^{-1} in the measured dispersion, in comparison with the value measured from the sky-subtracted spectrum. Thus, we conclude that the sky subtraction is not adversely affecting the velocity dispersion measurement. In the spectral order containing the Ca II triplet lines, the background spectrum is dominated by night sky emission lines, making it impossible to carry out a similar test for the Ca II dispersion.

Even when background subtraction is applied during the spectral extraction, the spectrum includes some residual light from the underlying galaxy disk. We used the results of the GALFIT decomposition of the WFPC2 image to estimate the fractional contribution of galaxy disk light to the ESI spectrum in the V band. We took the GALFIT models for the nuclear cluster and disk separately, convolved each with a Gaussian kernel of $\text{FWHM} = 1''.2$ to represent the likely seeing during the Keck observation, and measured the flux from each component within an aperture corresponding to the ESI slit ($0''.75 \times 1''$). Within this aperture, the disk contributes 26% of the total light. However, the background subtraction used in the spectroscopic extraction reduces this disk contamination substantially. The background regions used were $2''.5\text{--}5''.0$ on either side of the nucleus. We used the PC image itself to estimate the flux level in the background regions, since the GALFIT model does not include real structure such as dust lanes that are present in the actual sky background regions. We convolved the PC F606W image with the same Gaussian kernel and measured the counts in the exact background regions used in the ESI extraction. After subtraction of the mean background level, the remaining contribution of galaxy disk light to the ESI spectrum is only 10%. From the results of the background-subtraction test described above, we conclude that this small residual contamination of disk light in the ESI spectrum should not have a significant effect on the measured velocity dispersion of the cluster.

It is important to note that our measured value of σ_* is essentially the second moment of the cluster’s integrated line-of-sight velocity profile, which may contain a contribution from rotation as well as from random stellar motions within the cluster. Seth et al. (2008b) have found from high-resolution integral-field spectroscopic data that the nuclear cluster in NGC 4244 (an edge-on Scd galaxy) is rotating at 30 km s^{-1} , and if nuclear clusters are formed *in situ* by inflowing gas in the host galaxy disk, rapid rotation might be an important feature of nuclear clusters in general.

3.3. Emission-Line Spectrum

To measure the emission-line strengths and ratios, we carried out starlight subtraction on the wide-aperture spectral extraction using similar techniques, this time using a linear combination of a G8III–K3III giant and an A0V star spectrum to represent the stellar continuum. The starlight-subtraction fits were carried out over the ranges 4600–5300 Å and 6000–7000 Å, with the wavelengths of the narrow emission lines masked out in the fit. The results are shown in Figure 6. The starlight subtraction works reasonably well but results in an imperfect fit to the H α and H β absorption lines, leaving some spurious residual absorption in the starlight-subtracted spectrum. This residual absorption is the main source of uncertainty in the emission-line flux measurements described below, particularly for the very weak H β line.

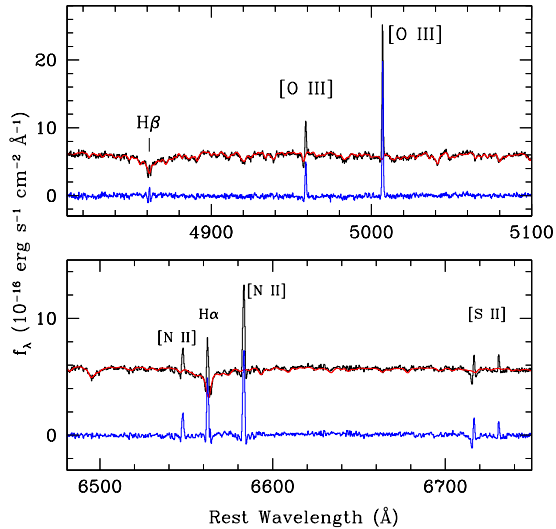


FIG. 6.— Starlight subtraction in the spectral region surrounding the $H\beta$ and $[O\ III]$ lines (upper panel) and the $H\alpha$ and $[N\ II]$ lines (lower panel). In each panel the spectrum of the nuclear cluster is shown in black, the best-fitting starlight model in red, and the starlight-subtracted spectrum in blue.

Emission line fluxes were measured by direct integration of the starlight-subtracted spectrum, with the results listed in Table 3. For $H\alpha$ and $H\beta$, we attempted to correct for the starlight-subtraction residuals by manually fitting a spline to the residual absorption profile and subtracting it from the spectrum; we performed several trial subtractions and the uncertainty range in the measured fluxes reflects the range of values measured in different trials. Although some line fluxes are highly uncertain, the results provide a clear emission-line classification for the nucleus. Figure 7 shows the location of the NGC 3621 nucleus in a line-ratio diagnostic diagram, in which it falls in the main Seyfert branch of the diagram. Thus, we classify NGC 3621 as a Seyfert 2 galaxy, and the optical spectrum adds further evidence that this galaxy contains an AGN.

From inspection of the two-dimensional ESI spectrum, the emission-line properties change systematically at a distance of roughly $3''.5$ from the nucleus. At this radius, the $[O\ III]/H\alpha$ and $[N\ II]/H\alpha$ ratios appear to drop substantially. If this change in emission-line ratios marks the boundary of the AGN-dominated narrow-line region, then the radius of this region is ~ 110 pc. Assuming a circularly symmetric narrow-line region on the plane of the sky, the ESI spectrum includes only $\sim 10\%$ of the total area of the emission-line region. Within this region, the emission-line surface brightness appears nearly constant in the ESI spectrum, thus our spectrum probably contains only about 10% of the total narrow-line flux of the AGN. It would be very useful to obtain a nuclear spectrum with an integral-field spectrograph, in order to better map out this emission-line region and obtain improved estimates of the total AGN luminosity.

The emission-line widths are unresolved in the ESI spectrum. We find $\text{FWHM} \approx 52\text{ km s}^{-1}$ for arc lamp lines observed through the same $0''.75$ slit width. The raw linewidths (not corrected for instrumental broadening) are 51 km s^{-1} for $[O\ III]\ \lambda 5007$ and 57 km s^{-1} for $[N\ II]\ \lambda 6583$, so the intrinsic linewidths must be substantially smaller than the instrumental resolution. Such narrow lines are exceptionally unusual for Seyfert 2 nuclei, even in low-mass host galaxies. Barth et al. (2008) used this same ESI setup to measure the linewidths

TABLE 3
EMISSION-LINE MEASUREMENTS

Line	Flux
$H\beta$	2.6 ± 1.3
$[O\ III]\ \lambda 5007$	22.4 ± 0.4
$H\alpha$	8.9 ± 2.4
$[N\ II]\ \lambda 6583$	13.0 ± 1.8
$[S\ II]\ \lambda 6716$	2.0 ± 0.5
$[S\ II]\ \lambda 6731$	1.8 ± 0.5

NOTE. — Emission-line fluxes are given in units of $10^{-16}\text{ ergs cm}^{-2}\text{ s}^{-1}$, and are corrected for Galactic reddening of $E(B-V) = 0.08$ mag (Schlegel et al. 1998). The flux scale has an unknown overall scaling uncertainty due to slit losses.

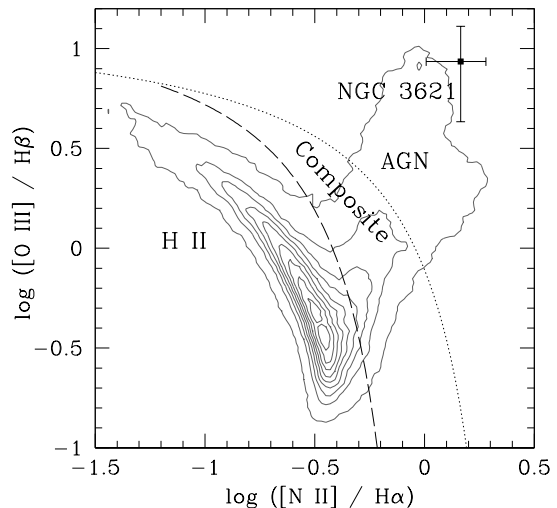


FIG. 7.— Emission-line diagnostic diagram illustrating the AGN classification of the NGC 3621 nucleus. Contours represent SDSS emission-line galaxies from Kauffmann et al. (2003). The dashed and dotted lines represent the classification boundaries of Kewley et al. (2006).

for a sample of low-mass Seyfert 2 galaxies selected from the Sloan Digital Sky Survey, and the smallest $[O\ III]$ width found was $\text{FWHM} = 66\text{ km s}^{-1}$ in the late-type spiral UGC 6192. NGC 3621 is so nearby that the ESI spectrum subtends only a small portion of the narrow-line region, and the linewidth might be substantially different if measured through a larger aperture.

The internal reddening toward the narrow-line region cannot be determined accurately, because of the very uncertain $H\beta$ flux measurement. From the Balmer line fluxes (corrected for Galactic extinction) we find $H\alpha/H\beta = 3.4 \pm 1.9$. This implies a possible range for the internal reddening from $E(B-V) = 0$ up to $E(B-V) = 0.6$ mag, assuming Case B recombination for the intrinsic Balmer-line ratios.

4. DYNAMICAL MODELING

As an initial approximation of the cluster's total mass, we use the virial theorem for a spherical, isotropic, and isolated system:

$$M_{\text{vir}} = f \frac{r_e \sigma_*^2}{G}. \quad (1)$$

Here, f is a dimensionless factor that depends on the density profile and velocity dispersion profile of the cluster, and σ_* is the line-of-sight velocity dispersion averaged over the density profile of the cluster. The numerical value of f is typically

~ 10 (e.g., Walcher et al. 2005) if the effective radius r_e is used as the cluster radius parameter. Taking $r_e \approx 4$ pc and $\sigma_* = 43$ km s $^{-1}$, this yields $M_{\text{vir}} \approx 1.7 \times 10^7 M_\odot$.

Though the virial theorem provides a rough estimate of the cluster mass, the precise value of the factor f depends on the density profile and velocity dispersion profile of the cluster. Additionally, the value of f would be affected if there are multiple components that significantly contribute to the mass of the cluster, such as a point mass in the form of a central black hole. In this case, the outskirts of the cluster blend smoothly into the galaxy disk, and the outer radius of the cluster is not well determined. For these reasons, in order to derive a more accurate cluster mass, as well as to determine constraints on the mass of the black hole, we compute dynamical models for the cluster based on the Jeans equation. This formalism allows us to model the structure of a star cluster with a two-component mass distribution including stars and a central point mass.

Similar to the virial theorem method, the total cluster mass as derived from the Jeans equation depends on its outer extent. However, determining the extent of the light that is gravitationally bound to the cluster is somewhat complicated by the fact that it is embedded in a disk. Particularly near the outermost radii, it is not entirely straightforward to distinguish between the light from stars bound to the cluster and the light due to the stars in the disk. In the GALFIT model for the cluster, 90% of the total cluster light in the multi-Gaussian model is contained within a projected radius of $0''.54$, or ~ 17 pc. To conservatively model the mass bound to the cluster, we use $r_{\text{out}} = 17$ pc as the fiducial outer radius of the cluster. All results described below from the dynamical modeling refer to the mass enclosed within this radius. We also note that the results described here refer to the mass of the nuclear cluster; the mass contributed by the galaxy disk component within this fiducial radius is not included in the dynamical mass results quoted below. Within a projected radius of 17 pc, the total light from the four GALFIT components corresponding to the cluster is equivalent to $L = 7.8 \times 10^6 L_{\odot, \text{V}}$.

The Jeans equation for the radial velocity dispersion, σ_r , is

$$r \frac{d(\rho_* \sigma_r^2)}{dr} = -\rho_*(r) \frac{GM(r)}{r} - 2\beta(r) \rho_*(r) \sigma_r^2. \quad (2)$$

The anisotropy of the stellar distribution is defined as $\beta = 1 - \sigma_\theta^2/\sigma_r^2$, the total dynamical mass enclosed within radius r is $M(r)$, and the three-dimensional luminosity density is $\rho_*(r)$. We use the boundary condition of $\rho_* \sigma^2 \rightarrow 0$ at the outer radius of the cluster, which we take to be 17 pc as described above.

To determine $\rho_*(r)$, we deproject the light distribution of the cluster via an Abel transformation. We use the results of the circularly symmetric GALFIT decomposition of the WFPC2 image as the model for the observed light distribution, assuming that the four narrowest GALFIT Gaussian components belong to the cluster. These Gaussian components are individually deprojected by Abel transformations, and the resulting $\rho_*(r)$ is the sum of these four deprojected functions.

To compare to the measured velocity dispersion of the cluster we integrate along the line of sight through the cluster:

$$\sigma^2(R) = \frac{2}{I_*(R)} \int_R^{r_{\text{out}}} \left(1 - \beta \frac{R^2}{r^2}\right) \frac{\rho_* \sigma_r^2 r}{\sqrt{r^2 - R^2}} dr, \quad (3)$$

where R is the projected radius on the plane of the sky and $I_*(R)$ is the surface brightness at R . We carry out the integration up to a radius of $r_{\text{out}} = 17$ pc, since this is the assumed outer radius of the cluster. Given the multi-component light

distribution determined from GALFIT, equations 2 and 3 cannot be solved analytically, so to obtain σ^2 we first numerically integrate the Jeans equation to obtain σ_r^2 , and then integrate this solution along the line of sight using equation 3 to obtain σ^2 .

Finally, to obtain the integrated line-of-sight velocity dispersion for comparison with the observed value, we average the line-of-sight velocity dispersion over the cluster, weighted by surface brightness:

$$\langle \sigma^2 \rangle = \frac{2\pi \int \sigma^2(R) I_*(R) R dR}{2\pi \int I_*(R) R dR}. \quad (4)$$

In the form above, the Jeans equation assumes spherical symmetry; given the small observed ellipticity of the light distribution of the cluster, as well as the fact that the circularly symmetric GALFIT model fits the cluster's radial profile well overall, this provides a good approximation to the dynamical mass. Further, this approach assumes that the cluster is non-rotating. Though the data do not give us any information on the rotation of this cluster, the small ellipticity can be interpreted as a small amount of flattening of the cluster due to rotation.

We model the mass distribution, $M(r)$, in terms of a component proportional to the stellar luminosity profile (assuming a spatially uniform stellar mass-to-light ratio) and a component representing the central point mass. This procedure allows us to examine a two-dimensional parameter space of the stellar mass-to-light ratio, M/L , and the central point mass, M_{BH} . As noted by Böker et al. (1999), an upper limit to M_{BH} can be determined by modeling the cluster in the limit that the stellar M/L approaches zero.

Since the cluster's mass and radius imply a half-mass relaxation time of order ~ 5 Gyr (Merritt 2008), and the cluster probably contains significant population components younger than this, the cluster may not be relaxed and it could have an anisotropic velocity dispersion. When scanning the parameter space, we fix the velocity anisotropy and assume it to be constant throughout the cluster. To explore the possible effects of anisotropy, we calculate models for three fixed values of the β parameter, $\beta = -1, 0$, and 0.5 . The values $\beta = -1$ and 0.5 correspond to ratios of tangential-to-radial velocity dispersions of $\sqrt{2} : 1$ and $1 : \sqrt{2}$, respectively.

In Figure 8, we show the resulting two-dimensional parameter space of M_{BH} vs. stellar mass-to-light ratio. For the specific case of isotropic velocity dispersion, the shaded band in Figure 8 shows the projected contours of line-of-sight velocity dispersions corresponding to the 1σ error range on our measurement of the cluster velocity dispersion of $\sigma = 43 \pm 3$ km s $^{-1}$. We see from Figure 8 that, in the limit that the stellar mass-to-light ratio approaches zero, we obtain a strict upper limit to the mass of the black hole, $3 \times 10^6 M_\odot$. Since we are averaging the velocity dispersion over the entire surface area of the cluster as in equation 4, this result turns out to be nearly independent of velocity anisotropy. We also find that, in the limit that $M_{\text{BH}} \rightarrow 0$, the stellar mass-to-light ratio is $1.4 \pm 0.2 (M_\odot/L_{\odot, \text{V}})$, again independent of the velocity anisotropy.

In Figure 9, we show the two-dimensional parameter space of black hole mass and integrated stellar mass within 17 pc. In the limit that $M_{\text{BH}} \rightarrow 0$, the stellar mass within 17 pc is constrained to be within $(0.95 - 1.2) \times 10^7 M_\odot$. This derived total stellar mass is on the larger end of the distribution of those measured by Walcher et al. (2005), due to the relatively high stellar velocity dispersion measured for NGC 3621. We also

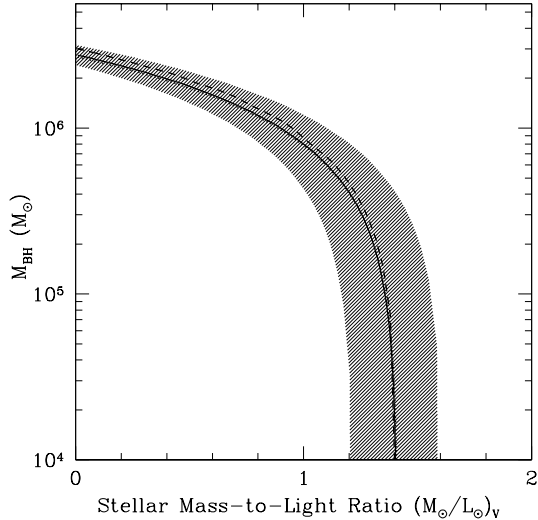


FIG. 8.— Dynamical modeling results. The curves show the locus of models yielding a line-of-sight velocity dispersion of $\sigma = 43 \text{ km s}^{-1}$ in the stellar (M/L_V) vs. M_{BH} plane. The dotted curves are for radially anisotropic models, the solid curves are for the isotropic models, and the dashed curves are for the tangentially isotropic models. The shaded band represents the 1σ uncertainty range on σ_* of 40-46 km s^{-1} for the isotropic model.

note that this result implies a value of $f \approx 6$ for the numerical factor in the virial theorem mass estimate (Equation 1).

We also computed a set of models in which the outermost Gaussian component from the WFPC2 GALFIT decomposition (with FWHM = $3''.1$ or 99.2 pc) was assumed to belong to the cluster rather than to the galaxy disk, to assess the impact that this choice has on the model results. The difference proved to be insignificant, because the width of this component is so large that only a small fraction of its mass lies within our fiducial 17 pc radius for the dynamical mass calculation. In the limit of $M_{\text{BH}} = 0$, the dynamical mass for the cluster changed by $< 1\%$ when the outermost Gaussian component was included as part of the cluster. Similarly, the upper limit to M_{BH} is unchanged if this component is added to the cluster model, and the error contours in Figures 8 and 9 are essentially unaffected by this change.

It bears repeating that in our mass estimates we assume that there is no rotational component contributing to the measured velocity dispersion. As argued above, this is a plausible assumption, although it is at this time not possible to determine what fraction of the observed velocity dispersion comes from ordered rotational motion. Any rotational motion will affect the above mass estimates, though determining by how much requires a full rotational model of the cluster, which depends not only on the rotational speed but also the inclination and eccentricity of the cluster. If the cluster were rapidly rotating *and* oriented with its rotation axis close to our line of sight, then our method would underestimate the true mass of the cluster and underestimate the upper limit to M_{BH} . With the data currently available, it is not possible to resolve the internal kinematics of the cluster or to constrain the cluster's rotation, or to measure the rotation speed or dispersion of the inner disk in the neighborhood of the cluster. However, it is unlikely that the cluster would be rotating in a nearly face-on orientation, since the host galaxy as a whole has an inclination of $i = 65.6^\circ$ (Paturel et al. 2003). The high-resolution kinematic study of the nuclear cluster in the edge-on galaxy NGC 4244 by Seth et al. (2008b) demonstrates that rotation can be

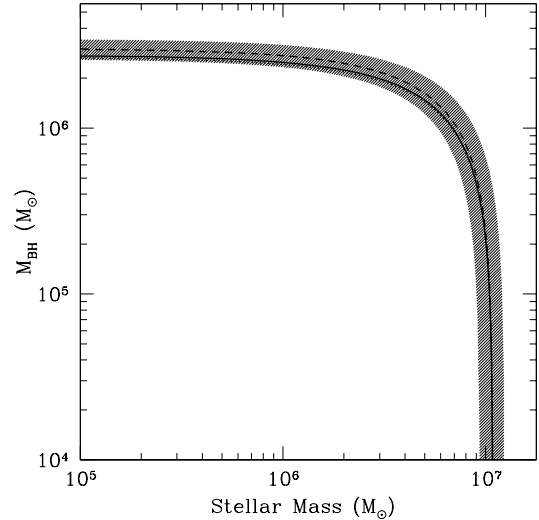


FIG. 9.— Dynamical modeling results. The curves show the locus of models yielding a line-of-sight velocity dispersion of $\sigma = 43 \text{ km s}^{-1}$ in the stellar mass vs. M_{BH} plane. Similar to Figure 8, the dotted curves are for radially anisotropic models, the solid curves are for the isotropic models, and the dashed curves are for the tangentially isotropic models. The shaded band represents the 1σ uncertainty range on σ_* of 40-46 km s^{-1} for the isotropic model.

dynamically important in nuclear clusters, and similar observations of the NGC 3621 cluster will be important for refining the cluster mass estimate.

Merritt (1987) has shown that a lower limit to the mass of a cluster can be derived from the virial theorem, based on the extreme limiting case in which all of the mass is contained at the central point of the cluster. This minimum mass is given by $GM_{\text{min}} = 3\sigma_*^2/\langle r^{-1} \rangle$, where $1/\langle r^{-1} \rangle$ is the harmonic mean radius of stars in the cluster and σ_* is the line-of-sight velocity dispersion. Averaged over the three-dimensional, deprojected light distribution, $\langle r^{-1} \rangle = 0.5 \text{ pc}^{-1}$, and the resulting lower limit to the cluster's dynamical mass is $\sim 2.6 \times 10^6 M_\odot$. This limit corresponds to our Jeans equation model for a cluster in which all of the mass is in the central point source, and the masses derived by these two methods turn out to be nearly identical. We interpret this in the following way. The minimum possible total mass of the cluster is found for the limit in which all of the mass is in a central point, whether calculated by the virial theorem or by more detailed Jeans equation modeling. As our Jeans equation modeling demonstrates, the lower limit to the mass of the cluster overall is the same as the upper limit to the mass of a black hole in the cluster. Therefore, the quantity $3\sigma_*^2/G\langle r^{-1} \rangle$ may be useful as a simple virial estimator of the maximum possible mass of a black hole in a star cluster. This could prove useful as a shortcut for deriving upper limits to black hole masses in larger surveys of nuclear clusters, and the limit derived in this way is substantially smaller than the total cluster mass derived from Equation 1.

In principle, the upper limit to M_{BH} could be lowered further if the stellar mass-to-light ratio could be constrained more accurately from multiband photometry and spectroscopy. From §2.3, the photometric data implies a V-band stellar mass-to-light ratio in the range $(1.4 - 2.0)M_\odot/L_{\odot,V}$. If we conservatively assume that $M/L_V > 1$ then the upper limit to M_{BH} would be $\sim 10^6 M_\odot$. Since our stellar mass estimates from photometry are very uncertain, we keep the extreme case of $M_{\text{BH}} < 3 \times 10^6$ as our best estimate of the upper limit to the black hole mass in this galaxy.

5. DISCUSSION

5.1. AGN Energetics

The AGN in NGC 3621 is faint and may be heavily obscured, and it is difficult to determine its bolometric luminosity. Satyapal et al. (2007) found a correlation between mid-infrared [Ne V] emission-line luminosity and bolometric luminosity for a small sample of nearby AGNs with well-sampled spectral energy distributions, and used this correlation to derive an estimate of L_{bol} for NGC 3621 based on its observed [Ne V] flux. They found $L_{\text{bol}} \approx 5 \times 10^{41}$ ergs s^{-1} , which is a substantial luminosity for an AGN in a late-type spiral. For comparison, NGC 4395 has $L_{\text{bol}} \approx 5 \times 10^{40}$ ergs s^{-1} and $L_{\text{bol}}/L_{\text{Edd}} \approx 10^{-3}$ (Moran et al. 1999; Peterson et al. 2005). If the infrared-based estimate of L_{bol} in NGC 3621 is correct, then the AGN must be almost entirely obscured in the optical; this would be consistent with its Type 2 classification and starlight-dominated continuum. Combining the value of L_{bol} from Satyapal et al. (2007) with our constraints on the black hole mass, we have $L_{\text{bol}}/L_{\text{Edd}} \gtrsim 10^{-3}$.

The [O III] $\lambda 5007$ flux measured from our ESI spectrum is $(22.4 \pm 0.4) \times 10^{-16}$ ergs s^{-1} after correcting for Galactic extinction. The uncertainty reflects only the statistical error in the extracted spectrum; additional error will arise from the unknown difference in slit losses between the galaxy and standard star observation. As described above in §3.3, the ESI spectrum probably includes only $\sim 10\%$ of the total [O III] flux from the AGN, so our measurement gives a lower limit to the true emission-line luminosity.

Heckman et al. (2004) find that for luminous Seyfert 1 galaxies, $L_{\text{bol}}/L([\text{O III}]) \approx 3500$ with a scatter of approximately 0.38 dex. Applying this [O III] bolometric correction to the lower limit for the [O III] luminosity of the NGC 3621 nucleus, we arrive at a lower limit of $L_{\text{bol}} > 4 \times 10^{40}$ ergs s^{-1} based on the optical spectrum. This is an order of magnitude lower than the estimated L_{bol} from the *Spitzer* spectrum. If the ESI spectrum represents 10% of the total nuclear [O III] flux, then the full [O III] luminosity would give an estimate of L_{bol} that is essentially consistent with the luminosity derived from the [Ne V] emission by Satyapal et al. (2007). Ultimately, the best constraints on the AGN energy budget and obscuration could be obtained from new X-ray observations, but there are none available at present. Perhaps most important, detection of a compact, hard X-ray source in the center of NGC 3621 would provide confirmation that it is genuinely an AGN.

5.2. Black Holes in Late-Type Spirals

Our primary result is that NGC 3621, which is a bulgeless or nearly bulgeless disk galaxy, contains a nuclear star cluster in which the maximum possible mass of a central black hole is $3 \times 10^6 M_{\odot}$. NGC 3621 is one of only a few examples of a bulgeless disk galaxy containing both a nuclear star cluster and a spectroscopically detected AGN. Under the standard assumption that the nuclear activity is driven by gas accretion onto a black hole, our results provide new evidence that some bulgeless spiral galaxies do contain low-mass central black holes. It is important to acknowledge that the detection of nuclear activity in NGC 3621 remains a good deal less secure than, for example, the well-studied Seyfert 1 nucleus in the late-type spiral galaxy NGC 4395. Still, the high-ionization [Ne V] emission found by Satyapal et al. (2007) and the Seyfert-type optical spectrum both provide a reasonable basis for classifying this object as an AGN. In this case, the low luminosity of the AGN is actually somewhat advan-

tageous: with no bright nuclear point source it is possible to obtain accurate measurements of both the stellar velocity dispersion and the structural properties of the nuclear star cluster. Such measurements would be far more difficult for a galaxy like NGC 4395, which contains a bright, unobscured AGN within its nuclear cluster.

Rossa et al. (2006) found an anticorrelation between morphological T -type and nuclear cluster mass, and a very weak correlation (with very large scatter) between total host galaxy B -band luminosity and nuclear cluster mass. Our dynamical models imply a stellar mass of $\sim 10^7 M_{\odot}$ for the NGC 3621 nuclear cluster if the black hole mass is small compared with the cluster's total mass. NGC 3621 has $T = 6.9 \pm 0.4$ and $\log(L_B/L_{\odot,B}) = 9.9$ (Paturel et al. 2003). With these values, and assuming a stellar mass of 10^7 for the NGC 3621 nuclear cluster, it is a fairly typical object in comparison with the Rossa et al. (2006) sample, falling within the scatter of both the cluster mass vs. T -type and cluster mass vs. host luminosity relationships. The only property of this cluster that appears unusual relative to previously studied nuclear clusters in late-type spirals is its larger velocity dispersion.

The location of NGC 3621 in the $M_{\text{BH}} - \sigma$ relation is shown in Figure 10. In this case, we use the sample compiled by Tremaine et al. (2002) for comparison, and include measurements or constraints on M_{BH} and σ_* for other late-type spiral galaxies (NGC 4395, IC 342, M33, and NGC 1042), for the dwarf elliptical NGC 205 (Valluri et al. 2005), and for the globular clusters G1 and ω Cen (Gebhardt et al. 2005; Noyola et al. 2008). For the late-type spirals, σ_* is taken to be the integrated line-of-sight velocity dispersion of the nuclear star cluster. The upper limit for NGC 3621 falls well above the $M_{\text{BH}} - \sigma$ relation extrapolated to low σ . Some studies of the low-mass end of the $M_{\text{BH}} - \sigma$ relation have suggested a possible flattening in slope at the low-mass end (Barth et al. 2005; Greene & Ho 2006b; Wyithe 2006), and it is important to test these claims with new dynamical measurements of black hole masses in low-dispersion galaxies, but our results do not provide any strong new constraints on the $M_{\text{BH}} - \sigma$ slope.

The upper limit to M_{BH} in NGC 1042 also lies considerably above the $M_{\text{BH}} - \sigma$ relation, but we note that this upper limit (from Shields et al. 2008) is simply the total dynamical mass of the cluster from Walcher et al. (2005, 2006), which is dominated by the stars in the cluster. The upper limit could be considerably tightened by calculating dynamical models with a central point mass in addition to an extended stellar component, as described above. Similarly, it would be interesting to compute upper limits based on this technique for all of the objects having stellar velocity dispersion measurements from Walcher et al. (2005), even for nuclear clusters that do not contain AGNs, since the more stringent upper limits that could be derived from this analysis could provide important new constraints on black hole demographics in late-type spirals.

With just a few nearby examples of very late-type spirals that are known to host AGNs, and just one object (M33) in which a massive black hole can be essentially ruled out, we have only a very incomplete picture of black hole demographics in late-type spirals. An important motivation for improving the black hole census in low-mass galaxies with small velocity dispersions is that the $M_{\text{BH}} - \sigma$ relation and black hole occupation fraction together encode key information about the mass scale of black hole seeds and the efficiency of seed formation, as discussed by Volonteri et al. (2008). Scenarios in

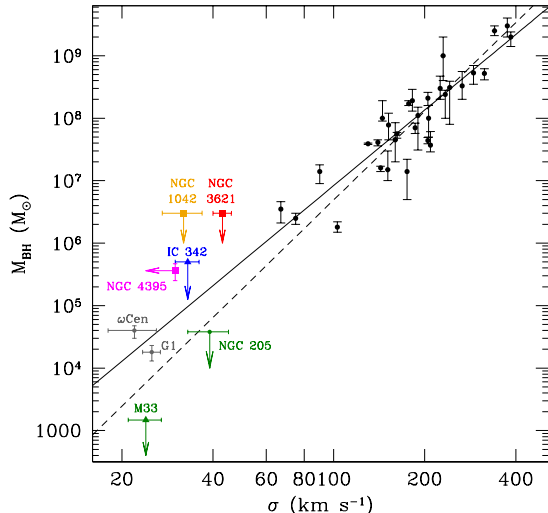


FIG. 10.— The $M_{\text{BH}}-\sigma$ relation including nuclear clusters in late-type spiral galaxies. Black circles are objects from the compilation of Tremaine et al. (2002). Filled squares represent nuclear clusters containing AGNs, including NGC 3621 (this work), NGC 4395 (Filippenko & Ho 2003; Peterson et al. 2005), and NGC 1042 (Walcher et al. 2005). Triangles represent nuclear clusters in late-type spirals without AGNs: IC 342 (Böker et al. 1999), M33 (Gebhardt et al. 2001). Globular clusters with stellar-dynamical detections of black holes are G1 (Gebhardt et al. 2005) and ω Cen (Noyola et al. 2008). The upper limit to the black hole mass in NGC 205 is from Valluri et al. (2005). Lines denote fits to the $M_{\text{BH}}-\sigma$ relation from Tremaine et al. (2002) (solid line) and Merritt & Ferrarese (2001) (dashed line).

which black holes begin as massive ($\sim 10^5 M_{\odot}$) seeds formed by collapse of low angular momentum gas at high redshift (Koushiappas et al. 2004; Lodato & Natarajan 2006) generally lead to low black hole occupation fractions in galaxies with small velocity dispersions. On the other hand, if black hole seeds are formed from the remnants of Population III stars and have masses of $\sim 100 M_{\odot}$, then the merger tree calculations described by Volonteri et al. (2008) predict high black hole occupation fractions in low-mass galaxies, but a steep slope for the lower end of the $M_{\text{BH}}-\sigma$ relation, with some galaxies hosting very tiny ($< 10^4 M_{\odot}$) black holes. While these models still do not incorporate all of the relevant physical processes involved in black hole growth (such as gravity-wave recoil kicks), it is becoming clear that a full census of black holes in dwarf and late-type galaxies can be a fundamentally important diagnostic of the mass scale of black hole seeds at high redshift. Much progress can be made through a combination of multiwavelength AGN surveys (e.g., Greene & Ho 2007; Gallo et al. 2008; Seth et al. 2008a; Satyapal et al. 2008; Desroches & Ho 2008) and improved stellar-dynamical searches for low-mass black holes, although a full census of the black hole content in low-mass galaxies is very far from being feasible at present.

Another possibility is that black holes in galaxies such as NGC 3621 might have formed at a later evolutionary stage, within the nuclear clusters themselves. The high densities of nuclear star clusters, as well as the likelihood of ongoing gas inflow from the host galaxy disk (Schinnerer et al. 2003; Milosavljević 2004), offer suggestions that nuclear clusters could be favorable environments for the formation and early growth of massive black holes. In sufficiently dense young star clusters with short dynamical friction timescales, intermediate-mass black holes could be formed by runaway collisions of massive stars in the cluster core (Portegies Zwart et al. 2004). This process is, however, un-

likely to operate within typical nuclear star clusters in disk galaxies. As noted by Walcher et al. (2005), the estimated dynamical friction timescale for a $100 M_{\odot}$ star to sink to the center of a nuclear cluster is longer than the star’s lifetime, and as a result the runaway process described by Portegies Zwart et al. (2004) would not occur. The same is true of NGC 3621; from Equation 1 of Portegies Zwart et al. (2004) we estimate a dynamical friction timescale of ~ 50 Myr for a $100 M_{\odot}$ star to sink to the cluster center, which is much longer than the lifetime of such a massive star. Still, more extreme conditions might occur during the early history of nuclear cluster formation, and the question of whether young nuclear star clusters might be favorable sites for black hole formation deserves further theoretical consideration.

6. SUMMARY AND CONCLUSIONS

Our main conclusions are as follows.

1. NGC 3621 has a Seyfert 2 optical spectrum, consistent with the AGN identification based on its mid-infrared spectrum by Satyapal et al. (2007). This adds further support for the hypothesis that a black hole is present.
2. For the nuclear star cluster, we find an effective radius of $r_e = 4.1$ pc, a line-of-sight stellar velocity dispersion of $\sigma_* = 43 \pm 3$ km s $^{-1}$, and an absolute magnitude of $M_V = -12.3$ mag (uncorrected for internal extinction). Simple estimates based on the available *HST* photometry suggest a stellar mass of $(1-3) \times 10^7 M_{\odot}$.
3. From two-dimensional image decomposition of 2MASS images, we find that the galaxy is dominated by an exponential disk, with at most a very faint possible pseudobulge component being present. We derive an upper limit of $M_K = -17.6$ mag to the luminosity of any bulge or pseudobulge component.
4. From stellar-dynamical modeling of the nuclear cluster, we find an upper limit to the black hole mass of $M_{\text{BH}} < 3 \times 10^6$. This result is insensitive to possible velocity anisotropy within the cluster. The upper limit is based on the extreme assumption of $M/L = 0$ for the stellar population. With improved photometric and spectroscopic observations it would be possible to better constrain the stellar mass-to-light ratio and reduce the upper limit on M_{BH} . Assuming that the cluster’s black hole mass is small in comparison with its stellar mass, the dynamical models give a stellar mass of $\sim 1 \times 10^7 M_{\odot}$ for the cluster.

These results add to the emerging body of evidence that some late-type, bulgeless galaxies do contain low-mass central black holes, and that black holes can be found inside some nuclear star clusters. It remains the case, however, that there are only a few late-type spirals in which the presence of a massive black hole has been either confirmed (based on nuclear activity) or ruled out (from dynamical modeling).

Further observations of the NGC 3621 nuclear cluster will lead to a more complete picture of the properties of this object. The most pressing observational need is for X-ray observations, to provide more definitive confirmation of the AGN interpretation and a better estimate of the AGN luminosity. Improved measurements of the stellar content of the nuclear

cluster can be obtained from high-resolution, high-S/N spectra extending farther to the blue than our ESI data, in addition to improved multi-band *HST* imaging covering the near-ultraviolet to near-infrared. Future extremely large ground-based telescopes with adaptive optics may make it possible to spatially resolve the kinematic substructure of the nuclear cluster, and this could lead to dramatically improved constraints on the black hole mass.

Research by A.J.B. and M.C.B. is supported by NSF grant AST-0548198, and research by L.E.S. is supported by NSF grant AST-0607746. We thank Rachel Kuzio de Naray for helpful conversations, and an anonymous referee for suggestions that improved this work. Data presented herein were obtained at the W.M. Keck Observatory, which is operated as a scientific partnership among Caltech, the University of California, and NASA. The Observatory was made possible by the generous financial support of the W.M. Keck Foundation. The authors wish to recognize and acknowledge the very sig-

nificant cultural role and reverence that the summit of Mauna Kea has always had within the indigenous Hawaiian community. We are most fortunate to have the opportunity to conduct observations from this mountain. This publication is based on observations made with the NASA/ESA Hubble Space Telescope, obtained from the Data Archive at the Space Telescope Science Institute, which is operated by the Association of Universities for Research in Astronomy, Inc., under NASA contract NAS 5-26555. These observations are associated with programs 5446, 9492, and 11080. This publication makes use of data products from the Two Micron All Sky Survey, which is a joint project of the University of Massachusetts and the Infrared Processing and Analysis Center/California Institute of Technology, funded by the National Aeronautics and Space Administration and the National Science Foundation. This research has made use of the NASA/IPAC Extragalactic Database (NED) which is operated by the Jet Propulsion Laboratory, California Institute of Technology, under contract with the National Aeronautics and Space Administration.

REFERENCES

- Abel, N. P., & Satyapal, S. 2008, *ApJ*, 678, 686
 Andredakis, Y. C., & Sanders, R. H. 1994, *MNRAS*, 267, 283
 Andredakis, Y. C., Peletier, R. F., & Balcells, M. 1995, *MNRAS*, 275, 874
 Baggett, S., Casertano, S., Gonzaga, S., & Ritchie, C. *Hubble Space Telescope Instrument Science Report WFPC2 97-10 (STScI)*
 Barth, A. J., Greene, J. E., & Ho, L. C. 2005, *ApJ*, 619, L151
 Barth, A. J., Greene, J. E., & Ho, L. C. 2008, *AJ*, in press
 Barth, A. J., Ho, L. C., & Sargent, W. L. W. 2002, *AJ*, 124, 2607
 Bell, E. F., McIntosh, D. H., Katz, N., & Weinberg, M. D. 2003, *ApJS*, 149, 289
 Blanton, M. R., & Roweis, S. 2007, *AJ*, 133, 734
 Böker, T., Laine, S., van der Marel, R. P., Sarzi, M., Rix, H.-W., Ho, L. C., & Shields, J. C. 2002, *AJ*, 123, 1389
 Böker, T., Sarzi, M., McLaughlin, D. E., van der Marel, R. P., Rix, H.-W., Ho, L. C., & Shields, J. C. 2004, *AJ*, 127, 105
 Böker, T., van der Marel, R. P., & Vacca, W. D. 1999, *AJ*, 118, 831
 Bruzual, G., & Charlot, S. 2003, *MNRAS*, 344, 1000
 Carollo, C. M., Stiavelli, M., de Zeeuw, P. T., & Mack, J. 1997, *AJ*, 114, 2366
 Carollo, C. M., Stiavelli, M., de Zeeuw, P. T., Seigar, M., & Dejonghe, H. 2001, *ApJ*, 546, 216
 Chabrier, G. 2003, *PASP*, 115, 763
 Desroches, L.-B., & Ho, L. C. 2008, *ApJ*, submitted
 Ferrarese, L., & Merritt, D. 2000, *ApJ*, 539, L9
 Ferrarese, L., et al. 2006, *ApJ*, 644, L21
 Filippenko, A. V., & Ho, L. C. 2003, *ApJ*, 588, L13
 Filippenko, A. V., & Sargent, W. L. W. 1989, *ApJ*, 342, L11
 Fioc, M., & Rocca-Volmerange, B. 1997, *A&A*, 326, 950
 Freedman, W. L., et al. 2001, *ApJ*, 553, 47
 Gallagher, J. S., Goad, J. W., & Mould, J. 1982, *ApJ*, 263, 101
 Gallo, E., Treu, T., Jacob, J., Woo, J.-H., Marshall, P. J., & Antonucci, R. 2008, *ApJ*, 680, 154 q
 Gebhardt, K., et al. 2000, *ApJ*, 539, L13
 Gebhardt, K., et al. 2001, *AJ*, 122, 2469
 Gebhardt, K., Rich, R. M., & Ho, L. C. 2005, *ApJ*, 634, 1093
 Gilliland, R. L. *Hubble Space Telescope Instrument Science Report ACS 2004-01 (STScI)*
 Greene, J. E., & Ho, L. C. 2006a, *ApJ*, 641, 117
 Greene, J. E., & Ho, L. C. 2006b, *ApJ*, 641, L21
 Greene, J. E., & Ho, L. C. 2007, *ApJ*, 667, 131
 Groves, B., Dopita, M., & Sutherland, R. 2006, *A&A*, 458, 405
 Heckman, T. M., Kauffmann, G., Brinchmann, J., Charlot, S., Tremonti, C., & White, S. D. M. 2004, *ApJ*, 613, 109
 Jedrzejewski, R. I. 1987, *MNRAS*, 226, 747
 Kannappan, S. J., & Gawiser, E. 2007, *ApJ*, 657, L5
 Kauffmann, G., et al. 2003, *MNRAS*, 346, 1055
 Kewley, L. J., Groves, B., Kauffmann, G., & Heckman, T. 2006, *MNRAS*, 372, 961
 Kinney, A. L., Calzetti, D., Bohlin, R. C., McQuade, K., Storchi-Bergmann, T., & Schmitt, H. R. 1996, *ApJ*, 467, 38
 Kormendy, J., & Richstone, D. 1995, *ARA&A*, 33, 581
 Koushiappas, S. M., Bullock, J. S., & Dekel, A. 2004, *MNRAS*, 354, 292
 Krist, J. 1993, *Astronomical Data Analysis Software and Systems II*, 52, 536
 Lodato, G., & Natarajan, P. 2006, *MNRAS*, 371, 1813
 MacArthur, L. A., Courteau, S., & Holtzman, J. A. 2003, *ApJ*, 582, 689
 Matthews, L. D., et al. 1999, *AJ*, 118, 208
 Merritt, D. 1987, *ApJ*, 313, 121
 Merritt, D. 2008, *ArXiv e-prints*, 802, arXiv:0802.3186
 Merritt, D., & Ferrarese, L. 2001, *ApJ*, 547, 140
 Merritt, D., Ferrarese, L., & Joseph, C. L. 2001, *Science*, 293, 1116
 Milosavljević, M. 2004, *ApJ*, 605, L13
 Moran, E. C., Filippenko, A. V., Ho, L. C., Shields, J. C., Belloni, T., Comastri, A., Snowden, S. L., & Sramek, R. A. 1999, *PASP*, 111, 801
 Nieto, J.-L., & Aurière, M. 1982, *A&A*, 108, 334
 Noyola, E., Gebhardt, K., & Bergmann, M. 2008, *ApJ*, 676, 1008
 O'Connell, R. W. 1983, *ApJ*, 267, 80
 Paturel, G., Petit, C., Prugniel, P., Theureau, G., Rousseau, J., Brouty, M., Dubois, P., & Cambresy, L. 2003, *A&A*, 412, 45
 Peng, C. Y., Ho, L. C., Impey, C. D., & Rix, H.-W. 2002, *AJ*, 124, 266
 Peterson, B. M., et al. 2005, *ApJ*, 632, 799
 Phillips, A. C., Illingworth, G. D., MacKenty, J. W., & Franx, M. 1996, *AJ*, 111, 1566
 Portegies Zwart, S. F., Baumgardt, H., Hut, P., Makino, J., & McMillan, S. L. W. 2004, *Nature*, 428, 724
 Rossa, J., van der Marel, R. P., Böker, T., Gerssen, J., Ho, L. C., Rix, H.-W., Shields, J. C., & Walcher, C.-J. 2006, *AJ*, 132, 1074
 Salpeter, E. E. 1955, *ApJ*, 121, 161
 Satyapal, S., Vega, D., Heckman, T., O'Halloran, B., & Dudik, R. 2007, *ApJ*, 663, L9
 Satyapal, S., Vega, D., Dudik, R. P., Abel, N. P., & Heckman, T. 2008, *ApJ*, 677, 926
 Schinnerer, E., Böker, T., & Meier, D. S. 2003, *ApJ*, 591, L115
 Schlegel, D. J., Finkbeiner, D. P., & Davis, M. 1998, *ApJ*, 500, 525
 Seth, A., Agüeros, M., Lee, D., & Basu-Zych, A. 2008a, *ApJ*, 678, 116
 Seth, A. C., Blum, R. D., Bastian, N., Caldwell, N., & Debattista, V. P. 2008b, *ApJ*, in press
 Sheinis, A. I., Bolte, M., Epps, H. W., Kibrick, R. I., Miller, J. S., Radovan, M. V., Bigelow, B. C., & Sutin, B. M. 2002, *PASP*, 114, 851
 Shields, J. C., Walcher, C. J., Böker, T., Ho, L. C., Rix, H.-W., & van der Marel, R. P. 2008, *ApJ*, 682, 104
 Skrutskie, M. F., et al. 2006, *AJ*, 131, 1163
 Spinoglio, L., & Malkan, M. A. 1992, *ApJ*, 399, 504
 Sturm, E., Lutz, D., Verma, A., Netzer, H., Sternberg, A., Moorwood, A. F. M., Oliva, E., & Genzel, R. 2002, *A&A*, 393, 821
 Tremaine, S., et al. 2002, *ApJ*, 574, 740
 Valluri, M., Ferrarese, L., Merritt, D., & Joseph, C. L. 2005, *ApJ*, 628, 137
 van den Bergh, S. 1976, *ApJ*, 203, 764
 Voit, G. M. 1992, *ApJ*, 399, 495
 Volonteri, M., Lodato, G., & Natarajan, P. 2008, *MNRAS*, 383, 1079
 Walcher, C. J., et al. 2005, *ApJ*, 618, 237
 Walcher, C. J., Böker, T., Charlot, S., Ho, L. C., Rix, H.-W., Rossa, J., Shields, J. C., & van der Marel, R. P. 2006, *ApJ*, 649, 692
 Walker, M. F. 1964, *AJ*, 69, 744
 Wehner, E. H., & Harris, W. E. 2006, *ApJ*, 644, L17
 Wyithe, J. S. B. 2006, *MNRAS*, 365, 1082